A One-dimensional Field Dislocation Mechanics Model Using Discontinuous Galerkin Method*

Ja'Nya Breeden[1,2], Dow Drake[1], Jay Gopalakrishnan[1], and Saurabh Puri†[3]

[1]Portland State University, PO Box 751, Portland, OR 97207
[2]Francis Marion University, PO Box 100547, Florence, SC 29502
[3]Microstructure Engineering, PO Box 5402, Portland, OR 97208

Abstract

A numerical solution strategy for a one-dimensional field dislocation mechanics (FDM) model using the Discontinuous Galerkin (DG) method is developed. The FDM model is capable of simulating the dynamics of discrete, nonsingular dislocations using a partial differential equation involving a conservation law for the Burgers vector content with constitutive input for nucleation and velocity. Modeling of individual dislocation lines with an equilibrium compact core structure in the context of this continuum elastoplastic framework requires a non-convex stored energy density. Permanent deformation and stress redistribution caused by the dissipative transport of dislocations is modeled using thermodynamics-based constitutive laws. A DG method is employed to discretize the evolution equation of dislocation density yielding high orders of accuracy when the solution is smooth. The trade-offs of using a high order explicit Runge-Kutta time stepping and an implicit-explicit scheme are discussed. The developed numerical scheme is used to simulate the transport of a single screw dislocation wall in the case of a non-zero applied strain.

1 Introduction

Dislocations are topological defects in crystals causing disorder in the otherwise perfect lattice. It is a well-known fact that plastic deformation in ductile crystals is caused by the gliding of a collection of dislocations on specific crystallographic slip planes. Physical properties such as strength, ductility, fracture, and fatigue resistance are manifestations of accumulation, collective motion and interaction of dislocations with other defects (vacancies, grain boundaries). Over the last few decades, significant progress has been made to understand the behavior of dislocations and related phenomena in crystals at different spatio-temporal

*Part of this work was conducted as an *undergraduate research experience* and was supported by the National Science Foundation under the REU Site grant CCF-1758006 and DMS-1912779.

†Corresponding author: saurabhpuri2005@gmail.com

scales (Kröner (1960), Mura (1963), Fleck et al. (1994), Fivel et al. (1997), Groma (1997), Acharya (2001), Gurtin (2002), Koslowski et al. (2002), Acharya (2003), Acharya (2004), Arsenlis et al. (2004), Roy and Acharya (2005), Deshpande et al. (2005), Acharya et al. (2010), Puri et al. (2011), Sandfeld et al. (2015), Zhang et al. (2015), Hussein and El-Awady (2016)).

This paper focuses on a field model of dislocation mechanics (FDM) developed by Acharya (2001), Acharya (2003), and Acharya (2010). FDM is a three-dimensional, physics-based model that can simulate the dynamics of non-singular, discrete dislocations as well as the related permanent deformation in the material with no restrictions on material or geometric nonlinearity. This continuum model represents dislocations using a second order tensor whose evolution follows a partial differential equation based on the conservation of Burgers vector content. Plastic distortion at the spatial scale of individual dislocations is solely derived from their motion and nucleation. Constitutive expressions for dislocation velocity, nucleation potential, and stress are thermodynamically derived from the stored energy density. Modeling of individual dislocations with a compact core in the context of this continuum elastoplastic framework requires a non-convex stored energy density. The model is flexible enough to include the atomically informed stored energy density (Gbemou et al. (2016)) as well as the bulk energy density corresponding to a collection of a few dislocations, if available.

A one-dimensional (1D) reduction of the small deformation FDM model with a non-convex description of crystal elasticity was derived in Acharya (2010). The equations of the 1D model represent the evolution of plastic shear strain in an infinitely long cylinder with a rectangular cross-section and were numerically implemented by Das et al. (2013) using an upwind finite difference scheme. The developed computational framework demonstrated the potential of the model in simulating the equilibrium core structure, motion and interaction of discrete walls of screw dislocations.

Zhang et al. (2015) utilized the computational scheme developed by Das et al. (2013) for a two-dimensional, finite element modeling of the behavior of few dislocations. The stored energy density was considered to be a sum of isotropic, linearly elastic energy which is a quadratic function of elastic distortion, a multi-well non-convex misfit energy to be a function of plastic distortion and an isotropic core energy to be a function of dislocation density tensor. Zhang et al. (2015) divided the two-dimensional body into elastic regions and elastoplastic regions. The elastoplastic regions were designated as "slip layers." They have finite thickness and represent crystallographic slip planes. A one-dimensional, scalar, time-dependent equation for plastic distortion is solved using an upwind finite difference scheme in each of these slip layers. The solution from the finite difference grid of the slip layers is then transferred to the finite element mesh to solve for stress equilibrium in the two-dimensional composite. This computational scheme was used to study different mechanisms such as, dislocation annihilation, dislocation dissociation, and supersonic dislocation motion.

Similarly, Gbemou et al. (2016) used a finite difference implementation of the 1D FDM framework to model planar dislocation lines and study physical phenomena, such as dislocation dissociation, and motion in hexagonal systems. They considered Peierls-Nabarro type misfit energy as well as a generalized planar stacking fault energy calculated from atomistic calculations.

The objective of this paper is to develop an advanced numerical scheme, capable of higher

order accuracy and varying spatial mesh sizes, that does not require a declaration of pre-existing slip layers for the modeling of discrete dislocation lines using the FDM framework. Since the evolution of dislocation density is governed by a conservation equation, a discontinuous Galerkin (DG) method emerges as a natural candidate for numerical treatment. The expectation is that the confinement of a dislocation to a slip plane is an outcome of the model rather than a predefined feature. As a first step to a full-fledged model in this direction, this paper uses a DG scheme to simulate a one-dimensional version of the FDM model using the open source finite element software NGSolve (see Schöberl et al. (2021)).

The DG method approximates the solution using a polynomial space on each element without interelement continuity constraints. The nonlinear partial differential equation for dislocation density has both convective and diffusive parts. Two different numerical strategies emerge, depending on how these parts are treated in the time discretization, as described in Section 3. The plastic distortion is obtained from the calculated dislocation density using the incompatibility equation. The developed framework is used to model the transport of an individual wall of screw dislocations. Note that in Das et al. (2013) and Zhang et al. (2015), a scalar evolution equation for the plastic distortion is solved using an upwind finite difference scheme. In this paper, we instead solve for the evolution of dislocation density (as in Gbemou et al. (2016)) and employ a DG scheme to do so. Due to its conservation properties and high order capabilities, DG methods are increasingly used in continuum mechanics, including mesoscopic modeling of dislocations (see e.g., Sandfeld et al. (2015)).

The remainder of this paper is organized as follows. A brief review of standard notation, the three-dimensional (3D) FDM model, and the derivation of the 1D model from the 3D model are given in Section 2. Numerical formulation of the non-dimensionalized form of the 1D model using a DG method is described in Section 3. The problem configuration and material parameters used in the simulations are described in Section 4.1 followed by a discussion of results in Section 4.2. Comparative analyses of the methods is facilitated by the reports of convergence rates in Section 4.3. We end with some concluding remarks in Section 5.

2 Model

The three-dimensional small deformation FDM model for modeling of discrete dislocations and its exact reduction to a one-dimensional form is derived in Acharya (2010). In this section, we review the equations of the model and present the derivation of the non-dimensionalized form of a 1D version.

2.1 3D model

Let $R \subset \mathbb{R}^3$ represent the reference configuration of a solid body under consideration with boundary ∂R. For a second-order tensor-valued function $\mathbf{A} : R \to \mathbb{R}^{3\times 3}$ and a vector-valued function $\mathbf{v} : R \to \mathbb{R}^3$, we define $\operatorname{curl} \mathbf{A}$ and $\mathbf{A} \times \mathbf{v}$, using the standard curl and cross products of vector fields, by requiring that

$$(\mathbf{A} \times \mathbf{v})^T \mathbf{c} = \left(\mathbf{A}^T \mathbf{c}\right) \times \mathbf{v} \quad \text{and} \quad (\operatorname{curl} \mathbf{A})^T \mathbf{c} = \operatorname{curl}\left(\mathbf{A}^T \mathbf{c}\right)$$

hold for all constant vectors $\mathbf{c} \in \mathbb{R}^3$. In rectangular Cartesian components, using the summation convention, $(\mathbf{A} \times \mathbf{v})_{im} = \varepsilon_{mjk} A_{ij} v_k$ and $(\operatorname{curl} \mathbf{A})_{im} = \varepsilon_{mjk} A_{ik,j}$, where a quantity with the comma subscript "$_{,j}$" refers to $\partial/\partial x_j$ applied to the quantity, and ε_{mjk} is a component of the third-order alternator. We shall also use a product of two second-order tensor fields $\mathbf{A} \,\mathbb{x}\, \mathbf{B}$ that gives a vector field whose Cartesian components are

$$(\mathbf{A} \,\mathbb{x}\, \mathbf{B})_i = \varepsilon_{ijk} A_{jm} B_{mk}. \tag{1}$$

As usual, we use a colon (:) between two second-order tensors to represent their contraction, i.e., in indicial notation, $\mathbf{A} : \mathbf{B} = A_{ij} B_{ij}$.

The model views dislocations as continuously distributed in the body R while it is deformed according to a smooth displacement field $\mathbf{u}$. Let $\mathbf{U}^e$ and $\mathbf{U}^p$ denote the elastic and plastic distortions. By the additive decomposition of total strain into elastic and plastic distortions, the equality $\nabla \mathbf{u} = \mathbf{U}^e + \mathbf{U}^p$ holds, where $(\nabla \mathbf{u})_{ij} = u_{i,j}$ in Cartesian coordinates. Let the symmetric part of $\mathbf{U}^e$ be denoted by $\boldsymbol{\varepsilon}^e$, i.e., $\boldsymbol{\varepsilon}^e = (\mathbf{U}^e + (\mathbf{U}^e)^T)/2$. Since $\mathbf{U}^e = \nabla \mathbf{u} - \mathbf{U}^p$, we may view $\boldsymbol{\varepsilon}^e$ as a function of $\mathbf{u}$ and $\mathbf{U}^p$,

$$\boldsymbol{\varepsilon}^e \equiv \boldsymbol{\varepsilon}^e (\mathbf{u}, \mathbf{U}^p) = \frac{1}{2}((\nabla \mathbf{u} - \mathbf{U}^p) + (\nabla \mathbf{u} - \mathbf{U}^p)^T). \tag{2}$$

Next, we proceed to specify the stress $\mathbf{T}$ as a function of $\boldsymbol{\varepsilon}^e$, introducing a constitutive assumption for the stored energy density, denoted by Ψ. Following Acharya et al. (2010) and Zhang et al. (2015), we consider Ψ to be a sum of three functions. The first is a function of symmetric part of the elastic distortion tensor $\Psi^e(\boldsymbol{\varepsilon}^e)$. The second is a function of the plastic distortion tensor $\eta(\mathbf{U}^p)$. The third is an isotropic function of dislocation density tensor $\boldsymbol{\alpha}$. Thus,

$$\Psi = \Psi^e (\boldsymbol{\varepsilon}^e) + \eta (\mathbf{U}^p) + \frac{\epsilon}{2} \boldsymbol{\alpha} : \boldsymbol{\alpha}. \tag{3}$$

Here

$$\epsilon = \frac{1}{4} \mu b^2 \tag{4}$$

is the core energy modulus, μ is the shear modulus, and b is the magnitude of Burgers vector. It is possible to incorporate various other expressions for Ψ into the model, such as those derived from atomistic calculations as shown in the incorporation of stacking fault energy in Gbemou et al. (2016). Using Ψ^e, we assume that the stress is given by the constitutive law

$$\mathbf{T} \equiv \mathbf{T}(\boldsymbol{\varepsilon}^e) = \frac{\partial \Psi^e}{\partial \boldsymbol{\varepsilon}^e}, \tag{5}$$

such that

$$T_{ij} = \frac{\partial \Psi^e}{\partial \varepsilon^e_{ij}} = 0 \quad \text{when} \quad \varepsilon^e_{ij} = 0. \tag{6}$$

Also, $\mathbf{T}$ satisfies the equilibrium equation,

$$\operatorname{div} \mathbf{T} = 0. \tag{7}$$

Inertia is ignored in this paper but can be easily incorporated if needed.

The fundamental work of Kröner (1960) connected the dislocation density tensor to the incompatible part of distortion through

$$\boldsymbol{\alpha} = -\operatorname{curl} \mathbf{U}^p. \tag{8}$$

The time derivative of $\mathbf{U}^p$, which we denote by $\dot{\mathbf{U}}^p$, is specified in terms of dislocation transport and nucleation, following Mura (1963), as follows:

$$\dot{\mathbf{U}}^p = (\boldsymbol{\alpha} \times \mathbf{V}) + \boldsymbol{\Omega}. \tag{9}$$

Here $\mathbf{V}$ is the dislocation velocity and $\boldsymbol{\Omega}$ corresponds to the nucleation of dislocation densities. Combining equations (9) and (8), we obtain the evolution equation of $\boldsymbol{\alpha}$,

$$\dot{\boldsymbol{\alpha}} = -\operatorname{curl} (\boldsymbol{\alpha} \times \mathbf{V}) - \operatorname{curl} \boldsymbol{\Omega}. \tag{10}$$

Equation (10) represents the conservation of Burgers vector content. In this paper, only mobility of a wall of screw dislocations is considered. Thus, the nucleation term ($\boldsymbol{\Omega}$) is set to zero.

We model the dislocation velocity $\mathbf{V}$ by

$$\mathbf{V} = \frac{1}{\widetilde{B}} \left(\mathbf{T} - \frac{\partial \eta}{\partial \mathbf{U}^p} + \epsilon \ \operatorname{curl} \boldsymbol{\alpha} \right)^T \mathbb{x} \, \boldsymbol{\alpha}, \tag{11}$$

for some positive function $\widetilde{B}(|\boldsymbol{\alpha}|) > 0$ called the dislocation drag coefficient. In (11), the product $\mathbb{x}$ is as defined in (1). This form of $\mathbf{V}$ is motivated by a study of dissipation. The dissipation (D) in the model is assumed to be the difference of rate of work done by external forces and the rate of change of stored energy in the body, so is modeled by

$$D = \int_R \left(\mathbf{T} : \nabla \dot{\mathbf{u}} - \dot{\Psi} \right) \, dv. \tag{12}$$

From physical considerations, we require $D \geqslant 0$. We shall now briefly see that the choice (11) yields $D \geqslant 0$ provided certain boundary fields can be neglected. We begin by differentiating Ψ, as given by (3), to get

$$\begin{aligned} \dot{\Psi} &= \frac{\partial \Psi^e}{\partial \boldsymbol{\varepsilon}^e} : \dot{\boldsymbol{\varepsilon}}^e + \frac{\partial \eta}{\partial \mathbf{U}^p} : \dot{\mathbf{U}}^p + \epsilon \boldsymbol{\alpha} : \dot{\boldsymbol{\alpha}} \\ &= \mathbf{T} : (\nabla \dot{\mathbf{u}} - \dot{\mathbf{U}}^p) + \frac{\partial \eta}{\partial \mathbf{U}^p} : \dot{\mathbf{U}}^p - \epsilon \, \boldsymbol{\alpha} : \operatorname{curl}(\boldsymbol{\alpha} \times \mathbf{V}), \end{aligned}$$

where we have used (5), the consequent symmetry of $\mathbf{T}$, and (10). After using (9) for $\dot{\mathbf{U}}^p$, we may substitute the resulting expression for $\dot{\Psi}$ into (12). Then, integrating the curl by parts,

$$\begin{aligned} D &= \int_R \left(\mathbf{T} - \frac{\partial \eta}{\partial \mathbf{U}^p} + \epsilon \ \operatorname{curl} \boldsymbol{\alpha} \right) : (\boldsymbol{\alpha} \times \mathbf{V}) \ dv - \int_{\partial R} \boldsymbol{\alpha} : ((\boldsymbol{\alpha} \times \mathbf{V}) \times \mathbf{n}) \ da \\ &= \int_R \left[\left(\mathbf{T} - \frac{\partial \eta}{\partial \mathbf{U}^p} + \epsilon \ \operatorname{curl} \boldsymbol{\alpha} \right)^T \mathbb{x} \, \boldsymbol{\alpha} \right] \cdot \mathbf{V} \ dv - \int_{\partial R} \boldsymbol{\alpha} : ((\boldsymbol{\alpha} \times \mathbf{V}) \times \mathbf{n}) \ da. \end{aligned}$$

This shows that whenever $\boldsymbol{\alpha} : (\boldsymbol{\alpha} \times \mathbf{V}) \times \mathbf{n}$ can be neglected on the boundary ∂R (which is the case in all the examples considered later in this paper), in order to obtain a non-negative dissipation, it is sufficient to choose $\mathbf{V}$ by (11).

Note that by (1), the Cartesian components of the vector $\mathbf{V}$ in (11) are given by

$$V_n = \frac{1}{\widetilde{B}} \varepsilon_{mnj} \left(T_{ij} - \frac{\partial \eta}{\partial U^p_{ij}} + \epsilon \left(\operatorname{curl} \boldsymbol{\alpha} \right)_{ij} \right) \alpha_{im}. \tag{13}$$

Following Zhang et al. (2015), one may set the dislocation drag coefficient $\widetilde{B}$ to

$$\widetilde{B} = B_m b^{m-1} \left| \boldsymbol{\alpha} \right|^m \tag{14}$$

where (as before, b is the magnitude of the Burgers vector) and B_m for some integer $m \in \{0, 1, 2\}$ is a given material constant. In the $m = 2$ case, note that components of the velocity may approach infinity (in regions where $\boldsymbol{\alpha}$ approaches zero). In this paper we focus only on numerical simulation of the $m = 1$ case.

To summarize the 3D model, we find two time-evolving functions $\mathbf{U}^p$ and $\boldsymbol{\alpha}$ using the system of two coupled equations

$$\dot{\boldsymbol{\alpha}} = - \operatorname{curl} \left(\boldsymbol{\alpha} \times \mathbf{V} \right), \qquad \dot{\mathbf{U}}^p = \boldsymbol{\alpha} \times \mathbf{V}, \tag{15}$$

where $\mathbf{V}$ is given by (11). When augmented by initial and boundary conditions, we obtain a system that is computationally treatable. One can envisage a computational strategy which updates $\boldsymbol{\alpha}$ and $\mathbf{U}^p$ using (15), given the current velocity field $\mathbf{V}$. Then the updated $\mathbf{U}^p$ can be used to solve for the displacement field $\mathbf{u}$ using $\boldsymbol{\varepsilon}^e = \boldsymbol{\varepsilon}^e(\mathbf{u}, \mathbf{U}^p)$ and $\operatorname{div} \mathbf{T}(\boldsymbol{\varepsilon}^e) = 0$, i.e., (2) and (7). Subsequently, the stress $\mathbf{T}$ is updated using (5) and used to compute the updated velocity $\mathbf{V}$ by (11). The process is then repeated. In the next section, we shall see a simplified one-dimensional model where (2), (5) and (7) are satisfied for all time, allowing us to focus on the issues in solving for the dislocation density using (15).

2.2 1D Model

The above-mentioned three-dimensional model can be reduced to a one-dimensional model under further assumptions.

We seek solutions to the three-dimensional model whose displacement $\mathbf{u}$ and plastic distortion $\mathbf{U}^p$ take the form

$$\mathbf{u}(x_1, x_2, x_3, t) = g(t) x_3 \, \boldsymbol{e}_2, \qquad \mathbf{U}^p(x_1, x_2, x_3, t) = \phi(x_1, t) \, \boldsymbol{e}_2 \otimes \boldsymbol{e}_3, \tag{16}$$

where $\boldsymbol{e}_i$ is the unit vector in the x_i-direction and $g(t)$ is some given function of time t and ϕ is to be determined (see Figure 1). It is immediate from (2) that (16) implies

$$\boldsymbol{\varepsilon}^e = \frac{1}{2} (\boldsymbol{e}_2 \otimes \boldsymbol{e}_3 + \boldsymbol{e}_3 \otimes \boldsymbol{e}_2) \, \gamma^e, \quad \gamma^e = g(t) - \phi(x_1, t). \tag{17}$$

Substituting the above expression for $\boldsymbol{\varepsilon}^e$ in (17) into the elastic contribution to the energy $\Psi^e(\boldsymbol{\varepsilon}^e)$, we define a function Q of the single scalar variable γ^e by

$$Q(\gamma^e) = \Psi^e(\frac{1}{2} (\boldsymbol{e}_2 \otimes \boldsymbol{e}_3 + \boldsymbol{e}_3 \otimes \boldsymbol{e}_2) \, \gamma^e). \tag{18}$$

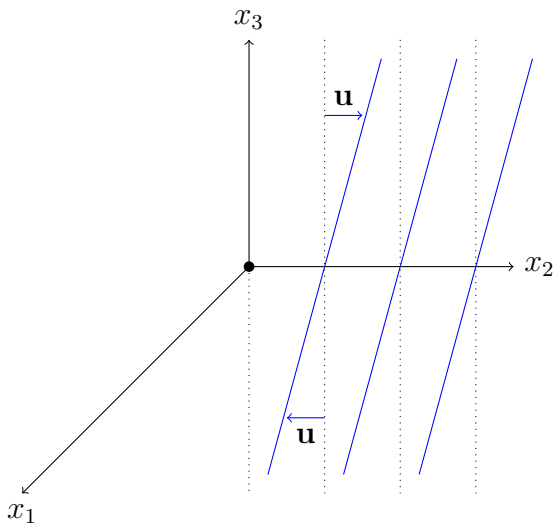

Figure 1: Schematic of the one-dimensional case, where dotted lines show the reference configuration and blue lines show the deformed configuration.

Clearly, (5) and (6) imply

$$\mathbf{T} = (\boldsymbol{e}_2 \otimes \boldsymbol{e}_3 + \boldsymbol{e}_3 \otimes \boldsymbol{e}_2)\, \tau(\gamma^e), \qquad \tau(\gamma^e) = 2Q'(\gamma^e). \tag{19}$$

By (17), γ^e depends only on x_1 and t, so we immediately verify that the equilibrium equation (7) trivially holds for all time for the above $\mathbf{T}$.

Another consequence of ansatz (16) and equation (8) is that $\boldsymbol{\alpha}$ only has a single nonzero component α_{22} and furthermore

$$\alpha_{22} = \partial_1 \phi. \tag{20}$$

Such a dislocation density tensor can represent a continuum of screw dislocations, invariant under translations in x_2 and x_3, with Burgers vector in the $\boldsymbol{e}_2$ direction.

To see how the model determines α_{22} as a function of x_1 and t, we examine the components of the dislocation velocity given by (13). Assuming that η is such that the (i,j)th component of $\partial\eta/\partial \mathbf{U}^p$ is zero whenever (i,j)th component of $\mathbf{U}^p$ is zero, we conclude that the only nonzero component of the velocity is in the x_1-direction and is given by $V_1 = -(\widetilde{B})^{-1}\left(\tau(\gamma^e) - \partial\eta/\partial U^p_{23} + \epsilon\, \partial_1 \alpha_{22}\right)\alpha_{22}$. Finally, the two equations of (15) imply

$$\partial_t \alpha_{22} = -\partial_1(\alpha_{22} V_1), \quad \text{and} \quad \partial_t \phi = -\alpha_{22} V_1, \tag{21}$$

respectively.

Henceforth, we write $x_1 = x$, $\alpha_{22}(x,t) = \alpha(x,t)$, $V_1(x,t) = V(x,t)$, $\partial_x = \partial_1$ to denote partial differentiation with respect to x, ∂_ϕ to denote partial differentiation with respect to ϕ, ∂_t to denote partial differentiation with respect to t, and abbreviate $\tau(\gamma^e)$ to τ when no confusion can arise. Then, the system we need to solve can be rewritten as

$$\begin{aligned} &\partial_t \alpha = -\partial_x(\alpha V), \\ &\partial_t \phi = -\alpha V, \end{aligned} \qquad \text{where } V = -\frac{1}{\widetilde{B}}\left(\tau - \partial_\phi \eta + \epsilon\, \partial_x \alpha\right)\alpha. \tag{22}$$

To summarize, *given* $g(t)$, η, $\widetilde{B}$, *and* ϵ, *setting* γ^e *by* (17) *and* $\tau(\gamma^e)$ *by* (19), *if we can find* α *and* ϕ *satisfying* (22), *then* $\mathbf{u}, \mathbf{U}^p$ *given by* (16), $\boldsymbol{\varepsilon}^e$ *given by* (17), $\mathbf{T}$ *given by* (19), *and* $\boldsymbol{\alpha} = \alpha \boldsymbol{e}_2 \otimes \boldsymbol{e}_2$ *will satisfy the three-dimensional model equations* (2), (5), (7), (8), *and* (15) *with* $\mathbf{V} = V\boldsymbol{e}_1$. This one-dimensional model forms a good testbed for various energy functions satisfying (6). The specification of τ in (22), due to (19), amounts to specification of Q in our framework.

For our numerical studies in later sections, we set η to 0 and choose any energy functional Ψ^e that leads, per (18), to

$$Q(s) = \frac{\mu\, s^2}{4\overline{\phi}^2}(s - \overline{\phi})^2, \tag{23}$$

where μ is the shear modulus and $\overline{\phi}$ is a material constant. Note that (6) requires that Q satisfy $Q'(s) = 0$ at $s = 0$. It is easy to check that this necessary condition is satisfied by the choice of Q in (23). By (19), this results in a *nonmonotonous relationship between the shear stress* τ *and elastic strain* γ^e, given by the following stress function introduced in Acharya (2010),

$$\tau(\gamma^e) = \frac{\mu}{2\left(\overline{\phi}/2\right)^2}\gamma^e\left(\gamma^e - \frac{\overline{\phi}}{2}\right)\left(\gamma^e - \overline{\phi}\right). \tag{24}$$

As proposed in Acharya (2010), we restrict the above form of $\tau(\gamma^e)$ for $\gamma^e \in [0,\ \overline{\phi}]$. For γ^e values falling outside of $[0,\ \overline{\phi}]$, the stress $\tau(\gamma^e)$ is set by taking a periodic extension, i.e., $\tau(\gamma^e)$ is set to $\tau(\gamma^e \pm n\overline{\phi})$ for an integer n. (This can alternately be viewed as extending Q periodically.) This periodically extended cubic stress implies the existence of minimum energy wells at $\gamma^e = \pm n\overline{\phi}$, $n = 0, 1, 2, \ldots$.

We complete this discussion of the one-dimensional model by a few remarks on $\widetilde{B}$ in (22), which in turn arises from (14). Note that using $\alpha = \partial_x\phi$, the one-dimensional version of (8), we can combine the two equations of (22) to

$$\partial_t\phi = \frac{|\partial_x\phi|^2}{\widetilde{B}}\left(\tau + \epsilon\,\partial_{xx}\phi\right) = \frac{|\partial_x\phi|^{2-m}}{B_m b^{m-1}}\left(\tau + \epsilon\,\partial_{xx}\phi\right) \tag{25}$$

since η is zero. Recall that only the case $m = 1$ is considered in this study; for simplicity we denote B_1 by B in the sequel. Then, the resulting equation, $\partial_t\phi = |\partial_x\phi|\left(\tau + \epsilon\,\partial_{xx}\phi\right)/B$ is often referred to as the *nonlocal level set model (NLS)*.

2.3 Nondimensionalization

We performed a nondimensionalization of the governing equations. This process results in reduction of roundoff error in our numerical methods and provides insights due the introduction of units which are intrinsic to the system being studied. To this end, we change variables as follows:

$$\hat{t} = t\frac{V_s}{b}, \quad \hat{x} = \frac{x}{b}, \quad \hat{\tau} = \frac{\tau}{\mu}, \quad \hat{\alpha} = \alpha b, \quad \hat{V} = \frac{V}{V_s}, \quad \hat{B} = B\frac{V_s}{\mu}, \quad \hat{\epsilon} = \frac{\epsilon}{\mu b^2},$$

where $V_s = \sqrt{\mu/\rho}$ is the elastic shear wavespeed of the material and ρ is its density. Note that $\hat{\epsilon} = \frac{1}{4}$ by the choice in (4).

Then, after simplifications, the equations of the one-dimensional model (22) take the following form in the terms of non-dimensional variables:

$$\begin{aligned} \partial_{\hat{t}}\hat{\alpha} &= -\partial_{\hat{x}}\left(\hat{\alpha}\hat{V}\right), \\ \partial_{\hat{t}}\phi &= -\hat{\alpha}\hat{V}, \end{aligned} \qquad \text{with } \hat{V} = -\frac{\hat{\alpha}}{\hat{B}\,|\hat{\alpha}|}\left(\hat{\tau} + \hat{\epsilon}\;\partial_{\hat{x}\hat{x}}\phi\right). \tag{26}$$

Recall that $\hat{\tau}$, as in (24), is given as a function of $g(t) - \phi(x,t)$. By (20), we also have

$$\partial_{\hat{x}}\phi = \hat{\alpha}, \tag{27a}$$

so we may eliminate either $\hat{\alpha}$ or ϕ to obtain equations for any one them. The equation for $\hat{\alpha}$ that emerges after using (27a) in the expression for dislocation velocity in (26), is

$$\partial_{\hat{t}}\hat{\alpha} = \partial_{\hat{x}}\left[\frac{|\hat{\alpha}|}{\hat{B}}\left(\hat{\tau} + \hat{\epsilon}\;\partial_{\hat{x}}\hat{\alpha}\right)\right]. \tag{27b}$$

Of course, we can also proceed as in (25) starting from (26) and eliminating $\hat{\alpha}$ to obtain an equation only for ϕ, namely

$$\partial_{\hat{t}}\phi = \frac{|\partial_{\hat{x}}\phi|}{\hat{B}}\left(\hat{\tau} + \hat{\epsilon}\;\partial_{\hat{x}\hat{x}}\phi\right). \tag{28}$$

The various approaches for solving the above equations of the 1D FDM model fall into two classes, a class of methods that numerically solves (28), and another that numerically solves (27). In Das et al. (2013), and Zhang et al. (2015), equation (28) was solved using the finite difference method. This approach has the advantage of having fewer equations than (27), which is particularly notable in higher dimensions (see e.g., Arora et al. (2020)), provided one can overcome the challenge of developing stable numerical methods for the Hamilton-Jacobi type system (28). Also, if the dislocation density $\hat{\alpha}$ is the primary quantity of interest that we wish to simulate, then this approach has the drawback of having to first compute $\hat{\alpha}$ and then compute ϕ from the computed $\hat{\alpha}$ by numerical differentiation, a process which results in loss of convergence order.

Another approach is to solve the system of equations (27a)–(27b) instead. This is done using a low order finite difference scheme in Gbemou et al. (2016). In our numerical scheme described in the next section, we will also adopt the approach of solving the system (27). The point of departure for us is that we use a DG method. One interest in such an approach lies in the possibility of getting high order direct numerical approximations of $\hat{\alpha}$ from the DG method. The drawback is that since $\hat{\tau}$ is best expressed using ϕ, not $\hat{\alpha}$, we must develop an intermediate step to recover ϕ from $\hat{\alpha}$ at each time step. It is critical that we not lose higher orders of accuracy in this intermediate step.

3 Numerical schemes

In this section, we study numerical schemes for solving the system (27) based on finite elements, specifically using discontinuous Galerkin schemes. Recall that the previously derived

1D model of dislocation density evolution was set in an infinite domain. We truncate the infinite 1D domain to the finite interval $(-L, L)$, restricting ourselves to simulation of α that is supported within this finite domain for duration of the simulation time $0 < \hat{t} < T$. For convenience, from now on, we drop the hats from the notation for the nondimensional quantities $\hat{x}, \hat{t}, \hat{\alpha}, \hat{\tau}$ and consider the following initial-boundary-value problem on the 1D domain $(-L, L)$:

$$\partial_x \phi = \alpha, \qquad |x| < L,\ 0 < t < T, \tag{29a}$$

$$\partial_t \alpha = \partial_x \left[\frac{|\alpha|}{\hat{B}} \left(\tau + \hat{\epsilon}\, \partial_x \alpha \right) \right], \qquad |x| < L,\ 0 < t < T, \tag{29b}$$

$$\alpha(x, 0) = \frac{\overline{\phi}}{2}(1 - \tanh^2 x), \qquad |x| \leqslant L,\ t = 0, \tag{29c}$$

$$\phi(x, 0) = -\frac{\overline{\phi}}{2}(1 - \tanh x), \qquad |x| \leqslant L,\ t = 0, \tag{29d}$$

$$\alpha(-L, t) = \alpha(L, t) = 0, \qquad |x| = L,\ 0 < t < T. \tag{29e}$$

In our numerical studies later, we choose the typical value of $\overline{\phi} = 0.05$ and simulate the evolution of dislocation densities in a domain of size $100b$, corresponding to the nondimensional domain half-length of $L = 50$. Note that the boundary conditions for ϕ are not included in (29). This is because the boundary value for ϕ is determined by the following ordinary differential equation obtained directly from (28), e.g., at $x = L$,

$$\partial_t \phi(L, t) = \frac{|\alpha(L, t)|}{\hat{B}} \left(\tau(L, t) + \hat{\epsilon}\, \partial_x \alpha(L, t) \right).$$

Clearly, by (29e), the right hand side is zero. Hence the value of ϕ at the right endpoint is constant, i.e., $\phi(L, t) = \phi(L, 0) = -\overline{\phi}/2(1 - \tanh L)$ for all $0 < t < T$. Since $1 - \tanh L$ is very close to zero for the values of L we have in mind, we work with the boundary condition

$$\phi(L, t) = 0, \qquad x = L,\ 0 < t < T. \tag{29f}$$

The specific forms of the initial and boundary values in (29) illustrate a typically studied scenario in FDM, but are immaterial to the construction of our numerical methods which admit general initial and boundary values. The approach we take to numerically solve (29) is to solve for α using (29b), (29c), and (29e), followed by solving for ϕ using (29a), (29d) and (29f) at the same time, and then repeating these two steps in a time stepping. Both these steps require spatial discretizations. A full discretization can then be constructed using a time stepping algorithm. These techniques will be described in detail in this section.

3.1 Spatial discretization

We begin by describing the spatial finite elements spaces we use for approximating α and ϕ. Both are approximated on the same mesh. Let $\mathcal{T}$ denote a mesh of the spatial domain $(-L, L)$, made up of $N + 1$ distinct vertices

$$-L = x_0, x_1, \ldots, x_{N-1}, x_N = L.$$

The i^{th} element of the mesh $\mathcal{T}$, denoted by K_i, is the open interval (x_{i-1}, x_i). The mesh size h is the width of the largest such interval. For any element K of $\mathcal{T}$, let $P_p(K)$ denote the space of polynomials in x, restricted to K, of degree less than or equal to a non-negative integer p. We approximate α using the piecewise polynomial space $V_h = \{v_h : v_h|_K \in P_p(K)\}$, also known as the DG space.

Since interelement continuity is not enforced for functions in this space, the value of a function $w \in V_h$ at a vertex x_i for $0 < i < N$ is not well defined. Yet, the left and right limiting values of w at such a vertex are well defined, respectively, by

$$w^-(x_i) = \lim_{x \to x_i^-} w(x) \quad \text{and} \quad w^+(x_i) = \lim_{x \to x_i^+} w(x).$$

Define the average $\{w\}_i$ and 'jump' $[\![w]\!]_i$ at a vertex x_i with $0 < i < N$ by

$$\{w\}_i = \frac{1}{2}\left(w^+(x_i) + w^-(x_i)\right), \qquad [\![w]\!]_i = w^+(x_i) - w^-(x_i). \tag{30}$$

The spatial approximation of dislocation density $\alpha(x,t)$, for each t, is of the form

$$\alpha_h(x,t) = \sum_{k=1}^{N(p+1)} \mathtt{a}_k(t)\theta_k(x) \tag{31}$$

where $\{\theta_k\}$ is a basis for V_h and the coefficients $\mathtt{a}_k$ are differentiable functions of time t. We will determine $\mathtt{a}_k$ through a system of ordinary differential equations formulated in Subsection 3.3.

Approximations to the plastic deformation are computed in the $(p+1)^{th}$ degree Lagrange finite element space satisfying the boundary condition (29f), namely $W_h = \{\psi_h \in C(-L, L) : \psi_h|_K \in P_{p+1}(K), \psi_h(L) = 0\}$. Noting that this space also has dimension $N(p+1)$, we consider approximations of $\phi(x,t)$ of the form (comparable to (31))

$$\phi_h(x,t) = \sum_{k=1}^{N(p+1)} \mathtt{b}_k(t)\psi_k(x) \tag{32}$$

where $\{\psi_k\}$ is a basis for W_h and the coefficients $\mathtt{b}_k$ are to be found.

3.2 Computing plastic deformation from dislocation density

In this subsection we focus on the computation of $\phi_h(x,t)$, given an approximation $\alpha_h(x,t)$ to the dislocation density at any time t. Considering (31) and (32), this amounts to computing $\{\mathtt{b}_k(t)\}$, given $\{\mathtt{a}_k(t)\}$. To do so, we discretize (29a) together with (29f).

Note that (29a) and (29f) can immediately be solved to obtain the exact solution

$$\phi = \mathcal{U}\alpha, \quad \text{where} \quad (\mathcal{U}\alpha)(x,t) = -\int_x^L \alpha(s,t)\, ds. \tag{33}$$

However, we need a more computationally convenient scheme to go from the coefficients $\{\mathtt{a}_k(t)\}$ to $\{\mathtt{b}_k(t)\}$. Therefore, we recast the problem as a Petrov-Galerkin approximation of

(29a)–(29f). Namely, for each fixed time t, given $\alpha_h(\cdot,t)$, we seek $\phi_h(\cdot,t) \in W_h$ satisfying

$$\int_{-L}^{L} (\partial_x \phi_h)\theta_h \, dx = \int_{-L}^{L} \alpha_h \theta_h \, dx \tag{34}$$

for all $\theta_h \in V_h$.

Equation (34) can be expressed in matrix-vector notation. Put the vectors of coefficients in (31)-(32) into time-dependent vectors $\mathtt{a}(t) = [\mathtt{a}_1(t), \ldots]^T$ and $\mathtt{b}(t) = [\mathtt{b}_1(t), \ldots]^T$. Define the time-independent matrices

$$A_{lm} = \int_{-L}^{L} (\partial_x \psi_m)\theta_l \; dx \qquad M_{lm} = \int_{-L}^{L} \theta_m \theta_l \; dx \tag{35}$$

Then (34) is the same as

$$A\,\mathtt{b}(t) = M\,\mathtt{a}(t).$$

Since the dimensions of V_h and W_h are equal, the matrix A is square. Moreover, it is invertible, since if $\alpha \equiv 0$, then choosing $\theta_h = \partial_x \phi_h$ in (34) gives $\partial_x \phi_h \equiv 0$, which implies that $\phi_h \equiv 0$ due to the boundary condition. Furthermore, since we have chosen the polynomial degrees so that $\partial_x \phi_h - \alpha_h \in V_h$, equation (34) implies that $\partial_x \phi_h - \alpha_h \equiv 0$. Since ϕ_h also satisfies the boundary condition (29f), it is the exact antiderivative of α_h, i.e.,

$$\phi_h = \mathcal{U}\alpha_h \tag{36}$$

using the exact formula $\mathcal{U}$ given in (33).

To summarize, by the Petrov-Galerkin equation (34), the vector of coefficients of $\phi_h(x,t)$, at any time t, is given in terms of the vector of coefficients of $\alpha_h(x,t)$, by

$$\mathtt{b} = A^{-1} M \mathtt{a}. \tag{37}$$

By appropriately choosing the basis functions θ_m, it is possible to perform this computation at asymptotically optimal cost.

3.3 Semidiscretization of dislocation density

Reversing the scenario of the previous subsection, we now proceed to compute α_h, assuming that an approximation to ϕ, namely $\phi_h(x,t)$, is available. For this, we develop a spatial discretization of (29b) subject to the boundary conditions (29e) and the initial condition (29c). Fixing a time t, we multiply (29b) by a test function $\theta \in V_h$ and integrate by parts on each mesh element $K_i = (x_{i-1}, x_i)$ to get

$$\int_{x_{i-1}}^{x_i} \left[(\partial_t \alpha)\, \theta + \frac{|\alpha|}{\hat{B}} \left(\tau + \hat{\epsilon}\, \partial_x \alpha\right) \partial_x \theta \right] dx - \frac{|\alpha|}{\hat{B}} \left(\tau\theta + \hat{\epsilon}\, (\partial_x \alpha)\theta\right) \Big|_{x_{i-1}}^{x_i} = 0. \tag{38}$$

Since an approximation to ϕ, namely $\phi_h(x,t)$ is available, τ can be approximated by $\tau_h(x,t) = \tau(g(t) - \phi_h(x,t))$. Note that the equation has a diffusive term and a convective term. Summing the previous equation over all elements, using α_h and τ_h in place of α and τ, and

denoting the convective flux by $F(x,t) = \hat{B}^{-1}|\alpha_h(x,t)|\,\tau_h(x,t)$ we obtain

$$\begin{aligned}0 = &\int_{-L}^{L} (\partial_t \alpha_h)\theta \; dx + \int_{-L}^{L} \frac{\hat{\epsilon}}{\hat{B}} |\alpha_h| \, (\partial_x \alpha_h) \, (\partial_x \theta) \; dx + \int_{-L}^{L} F \, \partial_x \theta \; dx \\ &- \sum_{i=1}^{N} \left(F^-(x_i)\theta^-(x_i) - F^+(x_{i-1})\theta^+(x_{i-1}) \right) \big) \\ &- \sum_{i=1}^{N} \frac{\hat{\epsilon}}{\hat{B}} \left(|\alpha_h^-(x_i)| (\partial_x \alpha_h)^-(x_i) \, \theta^-(x_i) - |\alpha_h^+(x_{i-1})| (\partial_x \alpha_h)^+(x_{i-1}) \, \theta^+(x_{i-1}) \right).\end{aligned}$$

Next, we use the standard Lax-Friedrichs numerical flux (see e.g., Cockburn and Shu (2001)) for approximating the convective fluxes across element interfaces. At x_i, it is given (using the notation introduced in (30)) by

$$\hat{F}_i = \{F\}_i + \frac{c}{2} [\![\alpha_h]\!]_i,$$

where $c = \max\{F'^{(-)}(x_i), F'^{(+)}(x_i)\}$ with $F' = \partial F / \partial \alpha$. The element interface terms arising from the diffusion term are approximated by the standard symmetric interior penalty form (see e.g. Arnold et al. (2002)). At a vertex x_i, this takes the form

$$P_i(\alpha_h, \theta) = \rho_d \, [\![\alpha_h]\!]_i \, [\![\theta]\!]_i - \{\partial_x \alpha_h\}_i \, [\![\theta]\!]_i - [\![\alpha_h]\!]_i \, \{\partial_x \theta\}_i,$$

in which we set the penalty parameter $\rho_d = 2p^2/h$. Using these approximations, and grouping into mass (m), convection (c), and diffusion (d) forms, we obtain the semidiscrete DG system,

$$m(\partial_t \alpha_h, \theta_l) + c^{g(t)-\phi_h}(\alpha_h, \theta_l) + d(\alpha_h, \theta_l) = 0, \tag{39}$$

where

$$m(\alpha_h, \theta_l) = \sum_{i=1}^{N} \int_{K_i} \alpha_h \; \theta_l \; dx, \tag{40}$$

$$c^{g(t)-\phi_h}(\alpha_h, \theta_l) = \sum_{i=1}^{N} \int_{K_i} F \; \partial_x \theta_l \; dx - \sum_{i=0}^{N} \hat{F}_i \; [\![\theta_l]\!]_i, \tag{41}$$

$$d(\alpha_h, \theta_l) = \sum_{i=1}^{N} \int_{K_i} \frac{\hat{\epsilon}|\alpha_h|}{\hat{B}} (\partial_x \alpha_h) \, (\partial_x \theta_l) \, dx + \sum_{i=0}^{N} \frac{\hat{\epsilon} \, |\{\alpha_h\}_i|}{\hat{B}} P_i(\alpha_h, \theta_l). \tag{42}$$

for any basis function θ_l of V_h. The superscript in $c^{g(t)-\phi_h}(\cdot,\cdot)$ serves to remind us of the dependence of F and $\hat{F}_i$ on $g(t) - \phi_h(x,t)$ through τ_h.

Employing the mass matrix defined in (35) and the coefficients $\mathtt{a}_k(t)$ in (31), the first term in (39) can be rewritten as the lth component of $M d\mathtt{a}/dt$. Let D denote the nonlinear operator on $\mathbb{R}^{(N+1)p}$ defined by $[D(\mathtt{a})]_l = d(\alpha_h, \theta_l)$ where we have again used the relationship between α_h and $\{\mathtt{a}_k\}$ in (31). Also connecting $\mathtt{b} \in \mathbb{R}^{(N+1)p}$ to ϕ_h by (32), we define $C^{\mathtt{b}}(\mathtt{a}, t) \in \mathbb{R}^{(N+1)p}$ for $t > 0, \mathtt{a}, \mathtt{b} \in \mathbb{R}^{(N+1)p}$ by $[C^{\mathtt{b}}(\mathtt{a}, t)]_l = c^{g(t)-\phi_h}(\alpha_h, \theta_l)$. Using these operators, (39) can be rewritten as

$$M \frac{d\mathtt{a}}{dt} + C^{\mathtt{b}}(\mathtt{a}, t) + D(\mathtt{a}) = 0, \tag{43}$$

which represents a system of ordinary differential equations (ODE) for $\mathtt{a} \in \mathbb{R}^{(N+1)p}$. Note that the system is not autonomous due to the t-dependence induced by $g(t)$.

3.4 Full discretization with time stepping

The full numerical method solves (29) by combining the discussions of Subsections 3.2 and 3.3. Specifically, we solve (39) using the particular choice of $\phi_h = \mathcal{U}\alpha_h$. Equation (37) leads us to select $\mathtt{b} = A^{-1}M\mathtt{a}$ in (43). Accordingly the ODE system for $\mathtt{a}(t)$ that we need to solve is

$$\frac{d\mathtt{a}}{dt} = f(\mathtt{a}, t), \qquad \text{with} \quad f(\mathtt{a}, t) = -M^{-1}\big(C^{A^{-1}M\mathtt{a}}(\mathtt{a}, t) + D(\mathtt{a})\big), \tag{44}$$

together with the initial conditions provided by (29c), translated to $\mathtt{a}(0)$. In this subsection, we present two options to solution. One leads to an explicit scheme, and the other to an implicit-explicit (IMEX) scheme.

3.4.1 The explicit Runge-Kutta option

At a discrete time step t_{n+1}, an explicit Runge-Kutta (RK) method (see e.g., Hairer et al. (1993)) produces an approximation $\mathtt{a}^{(n+1)}$ to the solution $\mathtt{a}(t_{n+1})$ of (44), assuming $\mathtt{a}(t_n)$ is known, using the following well-known formula:

$$\mathtt{a}^{(n+1)} = \mathtt{a}^{(n)} + \Delta t \sum_{i=1}^{s} b_i k_i,$$

where $\Delta t = t^{n+1} - t^n$,

$$\begin{aligned}
k_1 &= f(\mathtt{a}^{(n)}, t_n),\\
k_2 &= f(\mathtt{a}^{(n)} + a_{21}k_1\Delta t, t_n + c_2\Delta t),\\
k_3 &= f(\mathtt{a}^{(n)} + (a_{31}k_1 + a_{32}k_2)\Delta t, t_n + c_3\Delta t),\\
&\vdots\\
k_s &= f(\mathtt{a}^{(n)} + (a_{s1}k_1 + a_{s2}k_2 + \ldots + a_{s,s-1}k_{s-1})\Delta t, t_n + c_s\Delta t)
\end{aligned}$$

For a specific RK method, we must specify the number of stages, s, and the coefficients $a_{ij}(1 \leqslant j < i \leqslant s), b_i(i = 1, 2, \ldots, s)$ and $c_i(i = 2, 3, \ldots, s)$. These coefficients are commonly arranged in a lower triangular Butcher tableau, whose generic form, and the particular set of coefficients for the classical explicit RK4 scheme (which we shall use) are as follows, respectively:

$$\begin{array}{c|ccccc}
0 & & & & & \\
c_2 & a_{21} & & & & \\
c_3 & a_{31} & a_{32} & & & \\
\vdots & \vdots & & \ddots & & \\
c_s & a_{s1} & a_{s2} & \ldots & a_{s,s-1} & \\
\hline
 & b_1 & b_2 & \ldots & b_{s-1} & b_s
\end{array}
\qquad
\begin{array}{c|cccc}
0 & & & & \\
\frac{1}{2} & \frac{1}{2} & & & \\
\frac{1}{2} & 0 & \frac{1}{2} & & \\
1 & 0 & 0 & 1 & \\
\hline
\frac{1}{6} & \frac{1}{3} & \frac{1}{3} & \frac{1}{6}
\end{array}$$

All quantities needed to evaluate f (used to compute the intermediate k_i) have already been described. In order to conclude high order convergence for smooth solutions from the

well-known theory of RK methods, we cannot use naive approximations of the right hand side f (displayed in (44)). An important takeaway from this standard theory, as well as our numerical experience in computing dislocation densities using the RK4 scheme, is that replacing f by $f = -M^{-1}\big(C^{\mathtt{b}}(\mathtt{a},t) + D(\mathtt{a})\big)$ where the $\mathtt{b}$-vector of ϕ_h was precomputed for efficiency (or set by a time-lagged ϕ_h, or set by a common ϕ_h for every intermediate k_i-computation) can result in degradation of convergence rates. *It is critical to update the plastic distortion ϕ_h in every intermediate RK stage using the updated dislocation density α_h* to obtain high order accuracy for smooth solutions. This is accomplished by employing the f exactly as stated in (44).

3.4.2 The IMEX option

Since (39) contains both convective and diffusive terms, the above-described explicit scheme can be stable only when extremely small time steps (essentially dictated by the diffusion term) are taken. The IMEX option we now present forsakes higher order accuracy to gain larger time steps.

To describe the scheme, first define, in analogy with (42),

$$d^{\tilde{\alpha}_h}(\alpha_h,\theta_l) = \sum_{i=1}^{N}\int_{K_i}\frac{\hat{\epsilon}|\tilde{\alpha}_h|}{\hat{B}}(\partial_x\alpha_h)\,(\partial_x\theta_l)\,dx + \sum_{i=0}^{N}\frac{\hat{\epsilon}\,|\tilde{\alpha}_h^-(x_i)|}{\hat{B}}P_i(\alpha_h,\theta_l).$$

Then using the basis expansion (31) for α_h and for $\tilde{\alpha}_h = \sum_{k=1}^{N(p+1)}\tilde{\mathtt{a}}_k\theta_k(x)$, we define the *linear* operator $D^{\tilde{\mathtt{a}}}$ on $\mathbb{R}^{(N+1)p}$, for each fixed $\tilde{\mathtt{a}}$, by $[D^{\tilde{\mathtt{a}}}\mathtt{a}]_l = d^{\tilde{\alpha}_h}(\alpha_h,\theta_l)$. Clearly, the previously defined nonlinear $D(\cdot)$ is then given by $D(\mathtt{a}) = D^{\mathtt{a}}\mathtt{a}$. To solve (44), or equivalently,

$$M\frac{d\mathtt{a}}{dt} = -C^{A^{-1}M\mathtt{a}}(\mathtt{a}) - D(\mathtt{a}), \tag{45}$$

we use the strategy of time-lagging the convection term and splitting off an approximation of the diffusion term, $D(\mathtt{a})$, in such a way that the diffusion term can be implicitly handled: specifically, we approximate (45) by

$$M\frac{\mathtt{a}^{(n+1)}-\mathtt{a}^{(n)}}{\Delta t} + D^{\mathtt{a}^{(n)}}\mathtt{a}^{(n+1)} = -C^{A^{-1}M\mathtt{a}^{(n)}}(\mathtt{a}^{(n)}).$$

Rearranging, we obtain the IMEX scheme: it computes $\mathtt{a}^{(n+1)}$, given $\mathtt{a}^{(n)}$, by

$$\mathtt{a}^{(n+1)} = \mathtt{a}^{(n)} - \Delta t\big(M + \Delta t\, D^{\mathtt{a}^{(n)}}\big)^{-1}\big(C^{A^{-1}M\mathtt{a}^{(n)}}(\mathtt{a}^{(n)}) + D^{\mathtt{a}^{(n)}}\mathtt{a}^{(n)}\big). \tag{46}$$

Note that to implement this scheme, we assemble and invert the matrix $M + \Delta t\, D^{\mathtt{a}^{(n)}}$ at each timestep. Despite this extra cost, because stability can be obtained for IMEX with a timestep Δt proportional to h/p^2, we have observed good gains in computational efficiency on fine meshes, especially when $p = 1$. (In contrast, for explicit schemes, we need to choose a much smaller $\Delta t \lesssim Ch^2/p^2$ to attain stability.)

4 Numerical Simulations

4.1 Problem Setup

To model a moving wall of screw dislocations, we consider an initial profile of dislocation density α, and the corresponding ϕ, given by (29c) and (29d) respectively. Note that this choice of initial data for $\alpha(x,0)$ attains a maximum of $\overline{\phi}/2$ at $x=0$ and that (29a) holds at the initial time for the above choices of ϕ and α. In Figure 1, this choice of α corresponds to a dislocation density varying only in x_1 and concentrated near the x_2x_3-plane.

The motion of this dislocation wall is simulated in the case of a non-zero applied strain $g(t)$. The function $g(t)$ is ramped from zero to a fixed value and then kept constant for few time units. The exact profile for $g(t)$ is shown in the specific cases discussed in the next section.

The domain half-length $L = 50b$ was chosen sufficiently large to keep α near zero at the endpoints for the time frame of the simulation. The non-dimensional parameter values $\overline{\phi} = 0.05$, $\hat{\epsilon} = \frac{1}{4}$, and $\hat{B} = 1$ were chosen to model the dynamic behavior of aluminum, for which $b = 4.05\times10^{-10}$m, density $\rho = 2.7\times10^{3}\,\mathrm{kg/m^3}$ and shear modulus $\mu = 2.3\times10^{10}\,\mathrm{N/m^2}$. Since these trials required large simulation times, resulting in non-smooth solutions, the IMEX algorithm was used with order $p=1$, and mesh size $h = 0.0025b$. All the results are presented and discussed in terms of the non-dimensional units described in Section 2.3. No flux or slope limiting technique was found to be necessary in any of the presented simulations.

In some subsequent results, in addition to plots of α_h and ϕ_h, we also present calculated estimates of the observed peak velocity. A reasonably accurate estimate of the location of the peak value of α_h at a given timestep is obtained by first determining the mesh vertex at which α_h is maximized, then finding the critical point of the interpolating quadratic polynomial passing through the points associated with this vertex and its two neighbor vertices.

4.2 Results

In above-described set up, the implementation has been tested to verify that the initial profile of the dislocation wall does not change in the static case with $g(t) = 0$.

The main finding from our simulations is the result of applying a non-zero applied strain profile $g(t)$, shown in Figure 2a. In this case, the dislocation wall was observed to deform and move as a *localized* entity towards the right (Figure 2c). The evolution of ϕ is shown in Figure 2b. The velocity of the dislocation peak increases on ramping up the strain, reduces a little, and then becomes equal to a non-zero value when the strain is held constant (Figures 2e and 2f).

The effect of applied strain rate on the core evolution is shown in Figure 3. The profiles of the dislocation density α_h (Figure 3c) and the plastic deformation ϕ_h (Figure 3b), as well as the velocity of dislocation peak (Figure 3d) are observed to change significantly on changing the applied strain rate (and the corresponding final time). It is also observed that on increasing the strain rate the dislocation diffuses in the left direction.

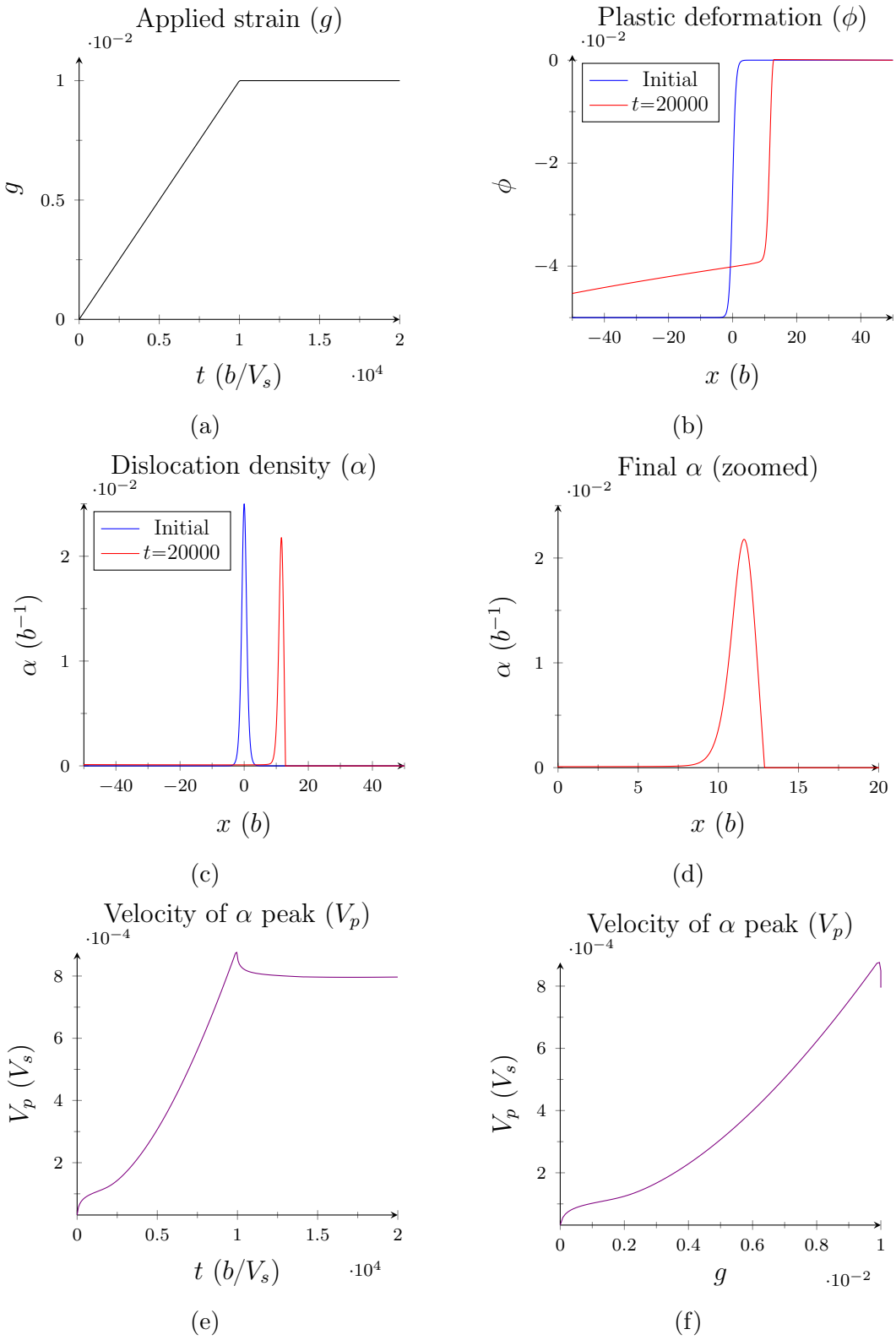

Figure 2: Effect of non-zero applied strain on the core structure with fixed boundary condition (a) applied strain profile, (b) plastic distortion, (c) dislocation density, (d) final α zoomed (e) peak velocity vs applied strain, (f) peak velocity vs time

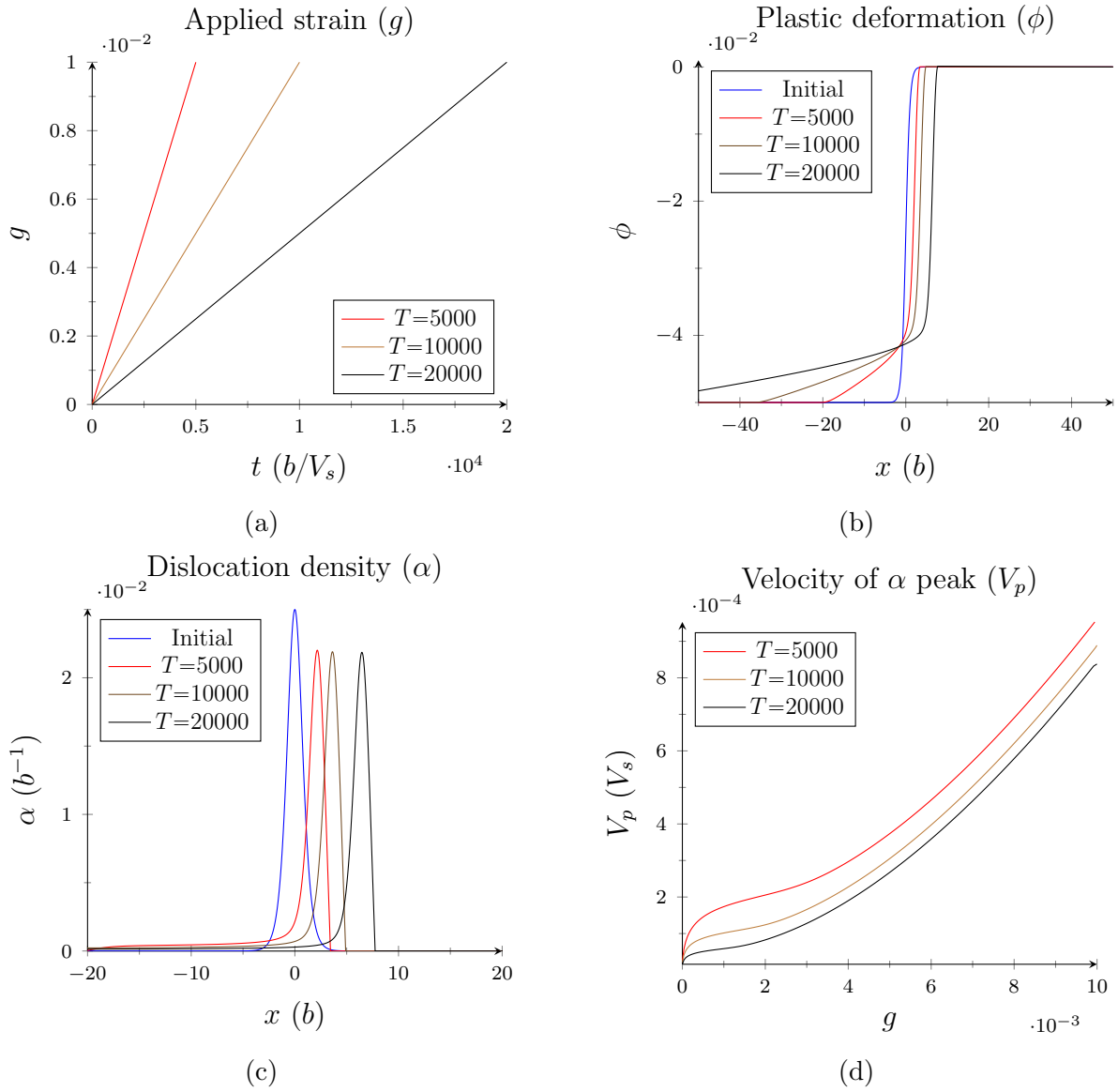

Figure 3: Effect of different applied strain rates and corresponding final times

4.3 Convergence rates

The purpose of this subsection is to report observed convergence rates of the proposed methods. For all convergence trials, we used an applied strain function $g(t)$ which ramped from zero at t=0 to a final value g_f at t=T, leading to a constant strain rate $\dot{g} = g_f/T$. Since the exact solution for this model with the periodically extended cubic internal stress is unknown, we estimated the numerically observed order of convergence from the L^2 distance of a computed solution to a reference solution (computed using the highest number of degrees of freedom we could afford).

Note that less smooth solutions are generally obtained for large applied strain rates or large values of the final time T (e.g., Figure 2d shows an α-profile that appears to be not continuously differentiable at the right base of the pulse). However, solutions exhibited high order smoothness when these parameter values were small. Accordingly, two sets of convergence studies were performed. The first set of studies were performed on parameter spaces which yielded fairly smooth solutions, for which the explicit RK4 method was appropriate. A study of convergence of the IMEX method was performed for a set of parameters yielding a less smooth α.

For comparison, we also implemented the finite difference method proposed in Das et al. (2013). This method computes an approximation to ϕ by discretizing (25) by finite differences and then computes an α-approximation from the ϕ-approximation via an upwind scheme based on velocity.

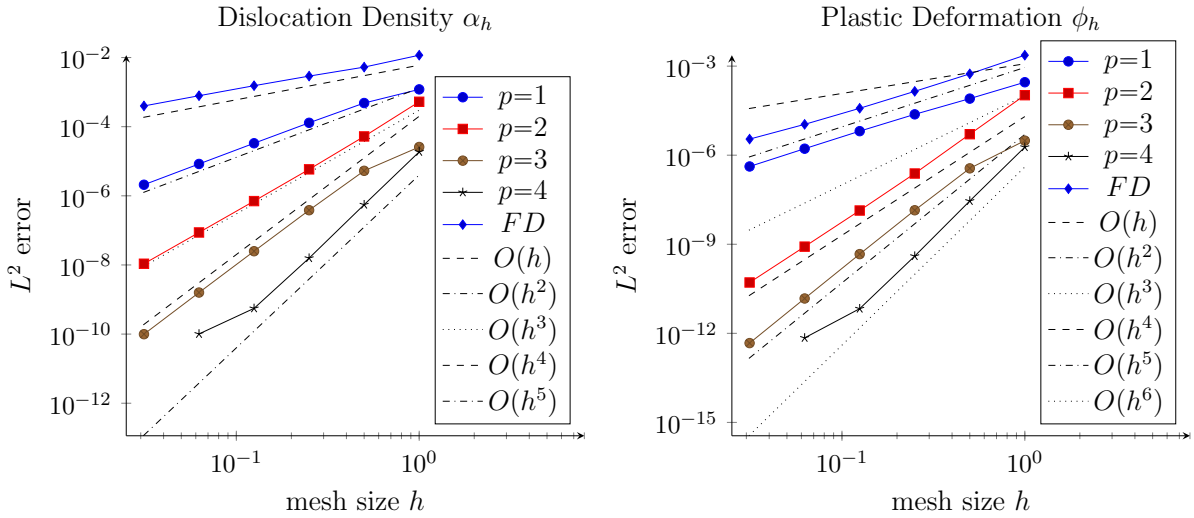

Figure 4: Explicit RK4 and finite differences (g_f=0.002, T=12)

Figure 4 shows the results for a study with T=12 and g_f=0.002. We see that the DG scheme together with the explicit RK4 time stepping converges to the reference solution at the expected rate of $O(h^{p+1})$ for α_h. The highest degree case on the finest mesh deviates from the perfect convergence curve probably due to its proximity to machine precision and ill-conditioning typical of higher degrees. As for ϕ_h, we observe that for $p > 1$, the convergence

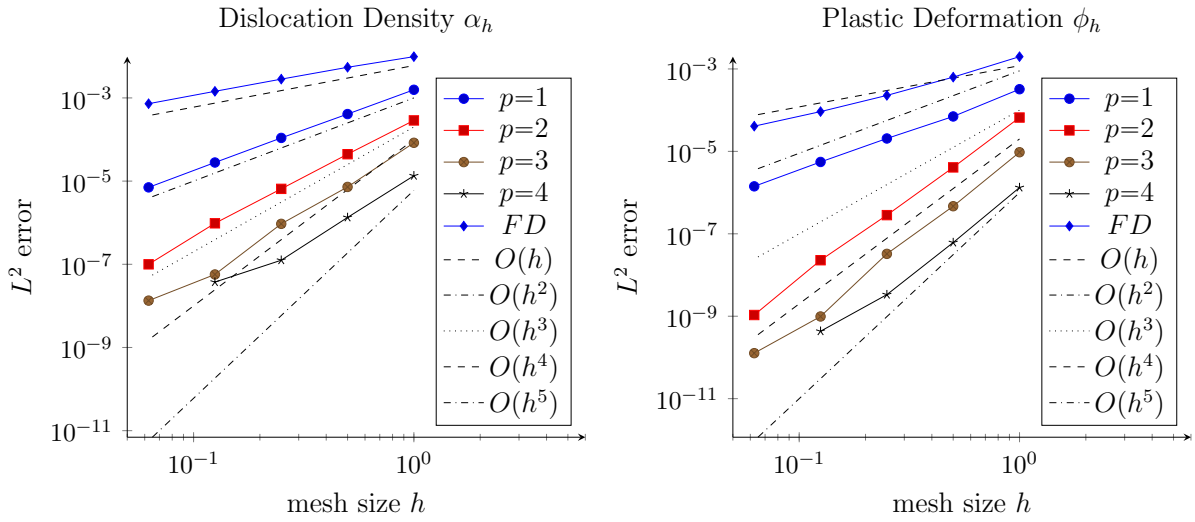

Figure 5: Explicit RK4 and finite differences (g_f=0.025, T=12)

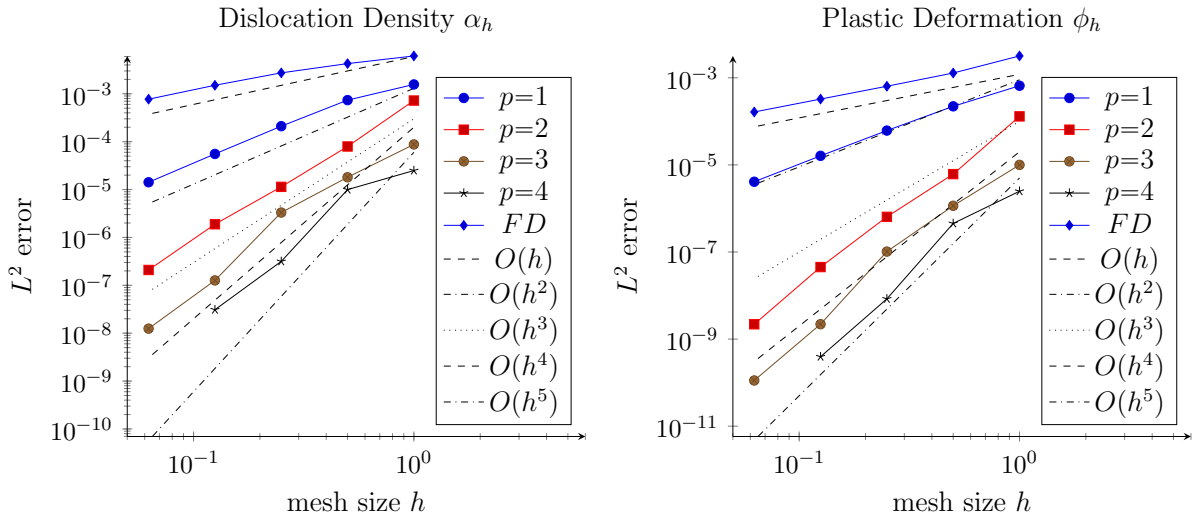

Figure 6: Explicit RK4 and finite differences (g_f=0.02, T=120)

rate of the DG scheme with explicit RK4 is approximately $O(h^{p+2})$. In contrast, the finite difference solution converges at a rate of $O(h)$ for α_h and approximately $O(h^2)$ for ϕ_h. Clearly the higher order of convergence attained by the DG scheme is preferable for the case of smooth solutions.

Figure 5 shows that a large strain rate results in loss of smoothness and hence impaired convergence (of the estimated errors which are nowhere near machine precision) for the higher order DG scheme with the explicit RK4 method. Figure 6 shows that if the strain rate is held constant, but T is increased significantly, the high order convergence is again impaired. This is in agreement with our observations that the solution seems to lose regularity over time. In these cases, we notice that the convergence rates for α_h are more immediately affected than those for ϕ_h by the loss of smoothness. This is agreement with the fact that α_h, being the spatial derivative of ϕ_h, has one less order of regularity.

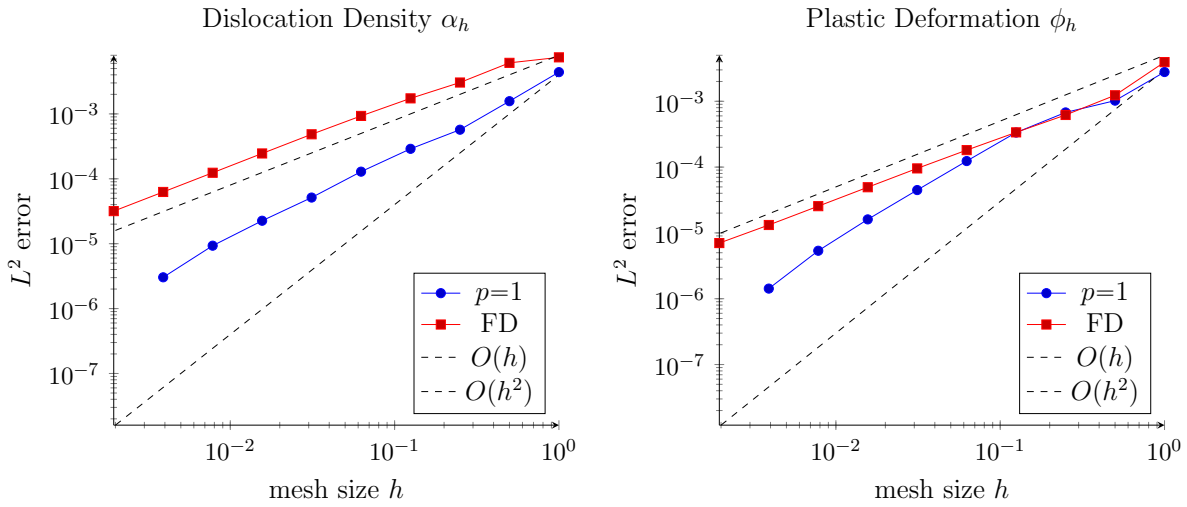

Figure 7: IMEX with p=1 and finite differences (g_f=0.01, T=1200)

We next consider the parameter space with a large T value. Attempts to solve the boundary value problem to large final times with this model using a high order polynomial space (without any limiting technique) resulted in overshoots and oscillatory errors. In such cases, the IMEX method is preferred, since further mesh refinement was needed to increase accuracy, and since the IMEX method is stable (for a given p) with a timestep $\Delta t \lesssim Ch$ (compared to the finite differences and explicit methods, which require a timestep $\Delta t \lesssim Ch^2$ for stability).

Figure 7 shows the results of a study with T=1280 and g_f=0.01, comparing the IMEX method with p=1 and the finite differences method. We see that the DG and finite difference solutions appear to converge to a common solution. The observed rate of convergence is $O(h)$ for the finite difference solutions and a slightly higher rate for the IMEX solution.

5 Conclusions

A discontinuous Galerkin finite element approach is used to model discrete dislocations in a continuum framework. The conservative numerical formulation is able to elucidate the physical phenomena of moving dislocation lines with compact cores in a crystal. Dislocation core evolution shows a strain-rate dependent response. As demonstrated in this paper, FDM has the potential for treating nonlinear core effects and incorporating stacking fault energy into the formulation. There is no need to introduce an inner cutoff radius to ignore the core effects.

The model studied here generates both smooth and nonsmooth solutions depending on the rate of applied strain and the simulation time. In cases when the exact solution for α is smooth, a higher order DG scheme combined with explicit RK4 time stepping is clearly the best choice, since it delivers very accurate solutions on coarse meshes, and exhibits a convergence rate of $O(h^{p+1})$, where p is the order of the spatial polynomial space. For less smooth solutions, the IMEX scheme is preferable. Both methods improve upon a prior finite difference scheme.

Acknowledgments

Saurabh Puri would like to acknowledge discussions with Amit Acharya (Carnegie Mellon University), Amit Das (Indian Institute of Technology), and Vincent Taupin (Universite de Lorraine/CNRS) regarding this paper.

References

A. Acharya. A model of crystal plasticity based on the theory of continuously distributed dislocations. *Journal of the Mechanics and Physics of Solids*, 49(4):761 – 784, 2001. doi: http://dx.doi.org/10.1016/S0022-5096(00)00060-0.

A. Acharya. Driving forces and boundary conditions in continuum dislocation mechanics. *Proceedings of the Royal Society of London A: Mathematical, Physical and Engineering Sciences*, 459(2034):1343–1363, 2003. doi: 10.1098/rspa.2002.1095.

A. Acharya. Constitutive analysis of finite deformation field dislocation mechanics. *Journal of the Mechanics and Physics of Solids*, 52(2):301 – 316, 2004. doi: http://dx.doi.org/10.1016/S0022-5096(03)00093-0.

A. Acharya. New inroads in an old subject: Plasticity, from around the atomic to the macroscopic scale. *Journal of the Mechanics and Physics of Solids*, 58(5):766 – 778, 2010. doi: http://dx.doi.org/10.1016/j.jmps.2010.02.001.

A. Acharya, K. Matthies, and J. Zimmer. Travelling wave solutions for a quasilinear model of field dislocation mechanics. *Journal of the Mechanics and Physics of Solids*, 58(12): 2043 – 2053, 2010. doi: http://dx.doi.org/10.1016/j.jmps.2010.09.008.

D. N. Arnold, F. Brezzi, B. Cockburn, and L. D. Marini. Unified analysis of discontinuous Galerkin methods for elliptic problems. *SIAM J. Numer. Anal.*, 39(5):1749–1779, 2002.

R. Arora, X. Zhang, and A. Acharya. Finite element approximation of finite deformation dislocation mechanics. *Computer Methods in Applied Mechanics and Engineering*, 367: 113076, 2020.

A. Arsenlis, D. M. Parks, R. Becker, and V. V. Bulatov. On the evolution of crystallographic dislocation density in non-homogeneously deforming crystals. *Journal of the Mechanics and Physics of Solids*, 52(6):1213–1246, 2004. doi: https://doi.org/10.1016/j.jmps.2003.12.007.

B. Cockburn and C.-W. Shu. Runge-Kutta discontinuous Galerkin methods for convection-dominated problems. *J. Sci. Comput.*, 16(3):173–261, 2001.

A. Das, A. Acharya, J. Zimmer, and K. Matthies. Can equations of equilibrium predict all physical equilibria? a case study from field dislocation mechanics. *Mathematics and Mechanics of Solids*, 18(8):803–822, 2013. doi: 10.1177/1081286512451940.

V. Deshpande, A. Needleman, and E. Van der Giessen. Plasticity size effects in tension and compression of single crystals. *Journal of the Mechanics and Physics of Solids*, 53(12): 2661–2691, 2005. doi: https://doi.org/10.1016/j.jmps.2005.07.005.

M. Fivel, M. Verdier, and G. Canova. 3d simulation of a nanoindentation test at a mesoscopic scale. *Materials Science and Engineering: A*, 234-236:923–926, 1997. ISSN 0921-5093. doi: https://doi.org/10.1016/S0921-5093(97)00362-6.

N. Fleck, G. Muller, M. Ashby, and J. Hutchinson. Strain gradient plasticity: Theory and experiment. *Acta Metallurgica et Materialia*, 42(2):475–487, 1994. ISSN 0956-7151. doi: https://doi.org/10.1016/0956-7151(94)90502-9.

K. Gbemou, V. Taupin, J. Raulot, and C. Fressengeas. Building compact dislocation cores in an elasto-plastic model of dislocation fields. *International Journal of Plasticity*, 82: 241–259, 2016. doi: http://dx.doi.org/10.1016/j.ijplas.2016.03.007.

I. Groma. Link between the microscopic and mesoscopic length-scale description of the collective behavior of dislocations. *Phys. Rev. B*, 56:5807–5813, Sep 1997. doi: 10.1103/PhysRevB.56.5807.

M. E. Gurtin. A gradient theory of single-crystal viscoplasticity that accounts for geometrically necessary dislocations. *Journal of the Mechanics and Physics of Solids*, 50(1):5–32, 2002. ISSN 0022-5096. doi: https://doi.org/10.1016/S0022-5096(01)00104-1.

E. Hairer, S. P. Nørsett, and G. Wanner. *Solving ordinary differential equations. I*, volume 8 of *Springer Series in Computational Mathematics*. Springer-Verlag, Berlin, second edition, 1993.

A. M. Hussein and J. A. El-Awady. Quantifying dislocation microstructure evolution and cyclic hardening in fatigued face-centered cubic single crystals. *Journal of the Mechanics and Physics of Solids*, 91:126–144, 2016. ISSN 0022-5096. doi: https://doi.org/10.1016/j.jmps.2016.03.012.

M. Koslowski, A. Cuitiño, and M. Ortiz. A phase-field theory of dislocation dynamics, strain hardening and hysteresis in ductile single crystals. *Journal of the Mechanics and Physics of Solids*, 50(12):2597–2635, 2002. doi: https://doi.org/10.1016/S0022-5096(02)00037-6.

E. Kröner. Allgemeine Kontinuumstheorie der Versetzungen und Eigenspannungen. *Arch. Rational Mech. Anal.*, 4:273–334 (1960), 1960.

T. Mura. Continuous distribution of moving dislocations. *Philosophical Magazine*, 8(89): 843–857, 1963.

S. Puri, A. Das, and A. Acharya. Mechanical response of multicrystalline thin films in mesoscale field dislocation mechanics. *Journal of the Mechanics and Physics of Solids*, 59 (11):2400–2417, 2011.

A. Roy and A. Acharya. Finite element approximation of field dislocation mechanics. *Journal of the Mechanics and Physics of Solids*, 53(1):143 – 170, 2005. doi: http://dx.doi.org/10.1016/j.jmps.2004.05.007.

S. Sandfeld, E. Thawinan, and C. Wieners. A link between microstructure evolution and macroscopic response in elasto-plasticity: Formulation and numerical approximation of the higher-dimensional continuum dislocation dynamics theory. *International Journal of Plasticity*, 72:1 – 20, 2015. doi: https://doi.org/10.1016/j.ijplas.2015.05.001.

J. Schöberl et al. NGSolve v6.2. `http://ngsolve.org`, 2021. Multiphysics finite element software. Last accessed 2021-08-16.

X. Zhang, A. Acharya, N. J. Walkington, and J. Bielak. A single theory for some quasi-static, supersonic, atomic, and tectonic scale applications of dislocations. 2015.